In situ thermal-microstructure characterization of a phase-transforming alloy satisfying cofactor conditions

Zhuohui Zeng [*,a,b], Xian Chen [b]

[a] Greater Bay Area, Shenyang National Laboratory for Materials Science, Tat Chee Avenue, Hong Kong
[b] Department of Mechanical and Aerospace Engineering, Hong Kong University of Science and Technology, Hong Kong

ARTICLE INFO

ABSTRACT

We establish an experimental platform to combine the differential scanning calorimetry (DSC) with an in situ observation of microstructure by differential interference contrast microscope (DInM). We carry out the experiment on a phase-transforming alloy $Au_{31}Cu_{24}Zn_{45}$ that closely satisfies the cofactor conditions - the strongest crystallographic compatibility constraints between phases. We confirm that the phase formation events observed by DInM agree well with the heat exchange profile characterized by DSC. We also observe different morphology of twins evolves differently, depending on the twin spacing. Through the quantitative analysis of various morphological domains in the temporal space, we discover that the scaling law between the twin evolution time and the fineness is linear, by which the characteristic transformation time for single variant martensite can be determined for this compatible martensite alloy as 0.636s.

Materials that exhibit reversible solid-solid phase transformation underlie a large category of functional materials for biomedical implants, smart actuation, caloric cooling and energy conversion. The reversibility and thermal hysteresis of the phase-transforming material strongly rely on the compatibility between crystal structures of austenite and martensite phases. It has been theorized that when the lattice parameters of the transforming crystal satisfy the cofactor conditions [1], both thermal hysteresis and functional degradation over numerous transformation cycles attain the minima. Therefore the cofactor conditions rationalize a design strategy for phase-transforming materials to achieve low-hysteresis and high-reversibility. In many transforming material systems, this design strategy has successfully guided the discovery of new functional alloys and oxides with nearly zero hysteresis [2–7] and million-cycles functional durability [8,9].

The cofactor conditions are supercompatibility conditions between austenite and martensite phases for reversible phase transformations. Mathematically, the cofactor conditions are a set of mathematical relations in terms of transformation stretch tensor and twinning parameters of martensite. Satisfaction of the cofactor conditions suggests that the twinned martensite can be fully compatible with the austenite through a stress-free interface depending on the fineness of the twin laminates.[1] The first example of an alloy that closely satisfies the cofactor conditions was reported in $Au_{30}Cu_{25}Zn_{45}$ shape memory alloy

[2], particularly, all types of twin systems including type I, type II and compound twins are equally close to achieve the supercompatibility. Consequently, the morphology of twinned martensite varies upon each of the transformation cycles, and the fineness of the martensitic microstructure changes from the grain boundary to far inside the grains.

In contrast, the conventionally twinned martensite morphology is quite different. According to the widely applicable crystallographic theory of martensite [10–12], the high-symmetry austenite and low-symmetry martensite are separated by habit planes, which are rigid and planar interfaces. Generically, the crystallographic theory predicts four normal directions for the habit planes adjoining which the laminated twins of martensite form at two volume fractions f and $1 - f \in [0, 1]$ for a specific pair of martensite variants. Experimental observations [13–17] and numerical simulations [18,19] repeatedly report these planar or piecewise planar interfaces consistent with the crystallographic theory. Near the habit planes, there exist stressed transition layers of the order of the twin spacing. The martensite twins exhibit branching from the martensite side of the interfacial region to meet up with the homogeneous austenite [20,21]. When the crystal satisfies the cofactor conditions, the morphological and crystallographic rigidity is much relaxed. First, the volume fraction of a pair of twinnable martensite variants can vary continuously from 0 to 1. Second, each of the martensite variants is compatible with the austenite through a

* Corresponding author
  E-mail address: zhzeng@connect.ust.hk (Z. Zeng).

rank-one connection [1] without any elastic transition layer. As a consequence, the martensite twins are unnecessarily branched into extremely fine laminates near the austenite/martensite interfaces. Some quantitative structural analysis by synchrotron X-ray diffraction [22] and electron backscatter diffraction [23] is conducted to study the compatible martensite microstructure. These experiments have verified that the formed twins are well connected by various rank-one connections with the twin spacing spreading in a wide range of length scales from hundreds of nanometers to sub-millimeters.

The formation and spatial distribution of coarse and fine compatible martensite twins seem random from cycle to cycle during the thermal induced phase transformation, but the evolution of microstructure suggests a certain scaling law, which has not yet been investigated. For a thermal induced phase transformation, the evolution of microstructure is closely related to the heat absorbed and released between the transforming bulk and its surroundings. When various compatible martensite twins exhibit equal formation tendency during the phase transformation, a time-space evolution law may be expected for the cofactor alloy. There were some works performed to observe the martensite microstructure formation corresponding to the local acoustic emission [24,25], which enlightened that the size of microstructure is related to the acoustic events through a power law in a coarse-grain polycrystalline Ni-Mn-Ga. But direct observation of thermal events during microstructure propagation at a reversible martensitic transformation has not yet been reported by far. The microstructure evolution and the accompanying energy behaviors of martensitic transformation are significant to understand and investigate the martensitic materials. In this paper, we integrate the differential interference microscopy (DInM) system to the differential scanning calorimetry system to perform an in situ thermal-microstructure study for the transforming Au-Cu-Zn alloy that closely satisfies the cofactor conditions. We propose a quantitative method to investigate the relationship between the fineness of microstructure and microstructure evolution behaviors.

A polycrystalline AuCuZn alloy was synthesized by casting in a tube furnace with nominal atomic composition 30 at% Au and 45 at% Zn. Then it was thermally treated at 650°C for 24 hours to achieve chemical homogeneity, finally quenched into ice water. Its actual atomic stoichiometry was characterized by energy dispersive X-ray micro-analysis (EDX, JSM-7100F JEOL) as $Au_{31}Cu_{24}Zn_{45}$, quite close to the reported AuCuZn alloy whose lattice parameters satisfy the cofactor conditions for all types of twin systems [2]. The alloy undergoes cubic to monoclinic phase transformation at $-45°C$. Under consecutive thermally

driven transformation cycles, this alloy exhibits a variety of martensitic twin structures similar to the unusual microstructure reported in reference [2]. We cut the ingot into a thin rectangular slice with a surface area of $1.6 \times 2.2mm^2$, thickness of $200\mu m$, and weight of 9.4mg. Then, we polished both top and bottom surfaces in room temperature to make sure they were flat in the austenite phase to provide good thermal contact with the thermal analysis instrument. We used 0.5 μm diamond grease to polish the sample in room temperature to make sure the surface of the specimen was flat in austenite phase. Fig. 1(c) shows that the austenite does not have macroscopic surface damages. The well-polished austenite is the reference configuration of our experiment. In addition, the flat austenite surface is considered as the reference configuration. Any surface reliefs due to martensitic transformation can be clearly revealed by DInM during the phase transformation.

The thermal-microstructure characterization was conducted by differential scanning calorimetry (TA Discovery DSC 250), which was integrated and synchronized with a DInM optical system (Nikon Ni-U) illustrated in Fig. 1(a). Tested sample surface can be characterized by the microscope through a transparent sapphire window (Fig. 1b), which was thermally isolated by the Discovery DSC Optical Microscope Accessory, provided by TA instruments. The inside and outside of DSC chamber was purged by 99.999% dry nitrogen gas to prevent frost during the thermal cycles below zero degree Celsius. Fig. 1(c) illustrates the thermal-microstructure results characterized by our experiment. The heat flow of the sample was measured by DSC at thermal loading rate of 7°C per minute, cycling between $-40°C$ and $-60°C$. Simultaneously, the microscope was continuously acquiring images at the speed of 15 frames per second (fps). From the thermal ramping rate given by DSC and the frame rate of the CCD camera, we calculate the temperature change per frame as $7/(60 \times 15) = 0.0078°C$, by which the microstructural evolution during phase transformation is synchronized with the heat flow along a universal time axis. More importantly, we can quantitatively study the thermal events of phase transformations corresponding to particular morphology.

By using the DInM optical system, subtle surface reliefs such as dimples, bumps, valleys, mountains can be revealed from the phase contrast images [26,27]. For crystalline materials with rich microstructure, the morphological configurations of interfaces and grain boundaries are more easily to be identified and segmented from the phase contrast images taken by the DInM. In the case that an alloy undergoing phase transformation from well-polished flat austenite to martensite with piece-wise linear surface reliefs, the surface regions of
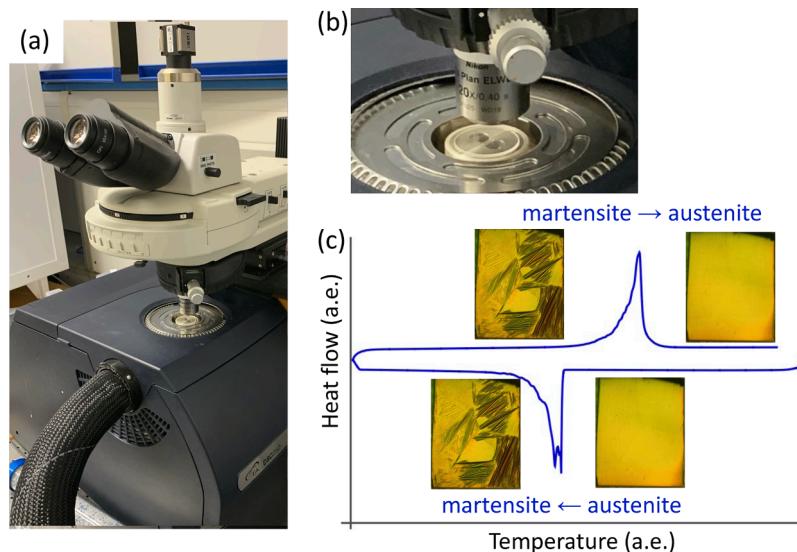

Fig. 1. (a) Experimental setup of the differential scanning calorimetry (DSC) analysis integrated with a DInM optical system through (b) a well-sealed transparent sapphire window. (c) An illustration of the thermal analysis by DSC and the corresponding microstructure characterized by the microscope.

austenite phase and variants of martensite can be segmented by the intensity values of the image. Suppose the field of view on the sample surface is $\mathscr{S} = [0, H] \times [0, W]$ where H and W are the numbers of horizontal and vertical pixels of an image captured during the experiment. The time-dependent DInM image is defined as

$$\mathscr{I} : \mathscr{S} \times [0, \infty] \to \mathbb{R}^+. \tag{1}$$

Note that for all pixels in $\mathscr{S}$ at the time t, the image given in (1) is normalized by $\max_{p \in \mathscr{S}} \mathscr{I}(p, t)$.

We used zero-mean normalized cross-correlation algorithm [28] to calculate a translation vector $[u(t), v(t)]$ such that the corresponding DInM image is corrected as $\widehat{\mathscr{I}}(p, t) = \mathscr{I}(p + [u(t), v(t)], t)$ to minimize the in-plane spatial shift between neighboring image frames caused by experimental vibrations from the thermal loading stage. In the temporal domain, we use an indexer $B : \mathscr{I}(\mathscr{S}, [0, \infty]) \to \{0, 1\}$ to identify whether a pixel $p \in \mathscr{S}$ undergoes a phase transformation by

$$B(p, t) = \begin{cases} 0, & \text{if } |\mathscr{I}(p, t + \tau) - \mathscr{I}(p, t)| \leq \epsilon \\ 1, & \text{else.} \end{cases} \tag{2}$$

In (2), the parameter $\tau = 1/fps$ second, that is the reciprocal of the frame rate of the camera, and a small constant ϵ is set as the threshold of intensity variation, over which the phase transformation is considered to take place at the pixel $p \in \mathscr{S}$. The value of ϵ is determined as the bandpass of the intensity fluctuations characterized by our microscope for reference configuration, which is the flat austenite surface.

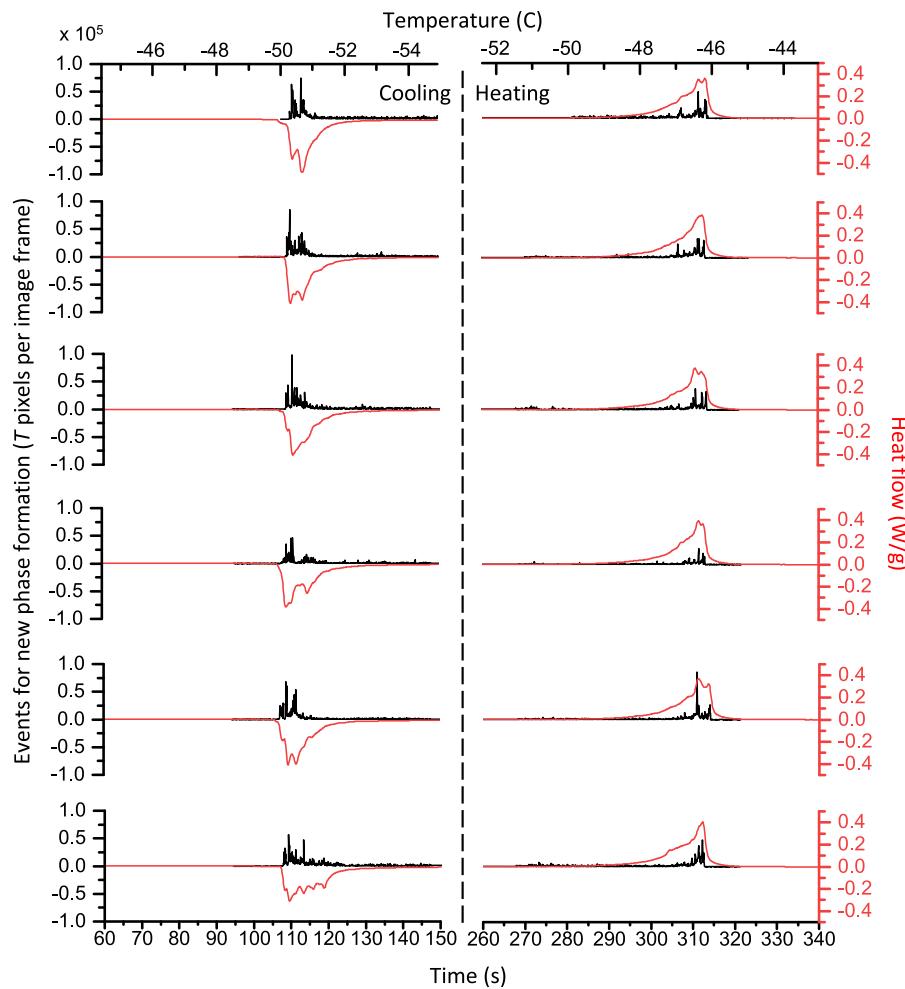The non-zero entries of B indexer suggest the phase transformation events during the thermal loading. The sum of its all entries presents the number of phase transformation events at an instant time t as

$$T(t) = \sum_{p \in \mathscr{S}} B(p, t). \tag{3}$$

The aforementioned $Au_{31}Cu_{24}Zn_{45}$ rectangular thin slice is thermally cycled between $-40°C$ and $-60°C$ at a rate of $7°C$ per minute, with microstructure synchronization for six complete phase transformation loops. By change of variable $\theta = \lambda t$ where $\lambda = 7°C$ per minute, the number of transformation events in (3) can be expressed as $T(\theta/\lambda) = \widehat{T}(\theta)$ for $-60°C < \theta < -40°C$. We used a monochromatic camera (IDS UI-3080CP Rev.2) to acquire the microstructure images with the frame rate of 15fps, while the DSC instrument was collecting the heat flow emitted/absorbed by the specimen. In our experiment, a complete phase transformation loop is counted from the isothermal austenite phase to martensite and back to austenite. We set the beginning of the experiment at austenite phase ($-40°C$) and let $Au_{31}Cu_{24}Zn_{45}$ went through 12 martensitic transformation processes in 6 consecutive thermal cycles.

Fig. 2 shows both microstructural events and thermal events over a temperature range that covers the phase transformation during heating and cooling processes. In all six transformation cycles, we observe that massive heat exchange (*i.e.* the peaks of heat flow) happens when an excessive amount of new phase form, revealed as the spikes of transformation events defined by (3). The temperature range from martensite start to finish during cooling, and from austenite start to finish during heating, spans 2°C with 4°C thermal hysteresis. As a comparison, typical

Fig. 2. Evolution of the phase transformation events and corresponding heat flow during thermal cycles.

shape memory alloys exhibit 15 to 40°C thermal hysteresis [29,30].

Fig. 2 shows that heat flow and transformation events are well correlated. The profile of heat flow measured from DSC matches the peaks of surface events detected by the optical microscope. Considering the specimen is very thin, *i.e.* nearly 20:1 area/thickness ratio, the DSC results are important evidence to support the fact that the surface events represent the formation of new phases in bulk. In the heating branch of $Au_{31}Cu_{24}Zn_{45}$, we observed that the heat flow curve is relatively smooth corresponding to continuously nucleated austenite phase. Noted that the thermal signal faded slightly slower than the convergence of transformation indexer because of the heat transfer retardance in the bulk specimen. In its cooling branch, we observed that the formation of martensite was step-wise, shown as the peak-splits of the heat flow corresponding to double bursts of transformation events within a narrow temperature window. Similar thermal-microstructure coupling was captured by acoustic emission measurement on NiMnGa [24], except that NiMnGa exhibits only one burst of transformation events during the martensitic transformation. This suggests that when the cofactor conditions are closely satisfied by lattice parameters of both phases, multiple low energetic martensite compatible microstructures may form in the material with different morphology. By our thermal-microstructure experiment, it is able to resolve the subtle variation of heat exchange events during the narrow transformation temperature range, and capture the formation of different martensite microstructure with sufficient temporal resolution.

To reveal the temporal evolution of various types of compatible martensite twinning structures, we trace the pixel wise evolution of martensite during phase transformation for all six thermal cycles during both heating/cooling processes. In a temporal sequence of image frames that fully cover the phase transformation events, for every pixel $p \in \mathscr{S}$, we solve

$$B(p,t) = 1, \text{ and } \frac{\partial B}{\partial t} > 0, \tag{4}$$

to obtain the ab initio moment of transformation, $t = t^*$, and plot each of the pixels in terms of their corresponding transformation moments in Fig. 3 during (a) cooling and (b) heating processes. The color mapping of Fig. 3 represents the microstructure evolution of each of the pixels in the image, which suggests that the dark blue regions transform prior to the bright yellow regions. By observation, it is found that the speed of transformation is different for the different morphological clusters: The coarser microstructure appears more suddenly and rapidly than the finer microstructure in cooling process, vice versa.

In each of the cooling cycles from austenite, we observed a variety of martensite microstructures with different twin spacings. This phenom-

enon is consistent with the report of the first martensitic material satisfying the cofactor conditions [2]. We classified the morphological domains according to the microstructure features within a sub-region manually selected from the image showing a fully developed martensitic microstructure. In a martensite image $\widehat{\mathscr{I}}$, for the intensity threshold $\epsilon > 0$, a morphological domain is defined as

$$\mathscr{M}_i = \{p : |\widehat{\mathscr{I}}(p) - I_i| < \epsilon, \text{ for } p \in \mathscr{S}\}, \tag{5}$$

where I_i is a selected value of intensity to identify the morphological domain within the image. The norm of the domain is determined as the total number of all included pixels denoted as $|\mathscr{M}_i|$. Among all heating/cooling cycles, we defined 12 morphological domains $\mathscr{M}_i$, $i = 1, \ldots, 12$ by (5), illustrated in Fig. 4(a) - (c). As seen, we presumably determined two morphological domains with different fineness for each of the transformation cycles: the red domain corresponds to a finer microstructure, while the black domain corresponds to a coarser microstructure. For each of the morphological domains, we trace the phase evolution density as

$$P_i(t) = \frac{1}{|\mathscr{M}_i|} \int_{t_0}^{t} \int_{\mathscr{M}_i} B(p,\tau) \, dp \, d\tau. \tag{6}$$

Here the time t_0 is determined as the start time when the phase transformation has not yet occurred in the material for the morphological domain $\mathscr{M}_i$, that is $P_i(t_0) = 0$. Suppose t_1 is the time when all pixels in $\mathscr{M}_i$ has transformed, for $t > t_1$, $P_i(t) = 1$. Fig. 4(d) shows the evolution of new phase per pixel in each of the selected morphological domains during both heating/cooling processes. We observed that the coarser microstructure (black) evolves more rapidly and abruptly than the finer microstructure (red). We can also observe the avalanches for the microstructure formation at different twin spacing. To observe the microstructure evolution of $Au_{31}Cu_{24}Zn_{45}$ clearly, dual beam-shear DInM [27] was employed to characterize the surface topography evolution quantitatively, and we present the results in the supplementary video. Although various twin systems may form during the phase transformation, the twinning planes can be classified into three categories: {100} compound twin wall, {110} type I/II twin wall. In principle, the crystallographically equivalent twin walls have the same planar density, thus the same twin wall energy. Since all twins are rank-one connected, there is no elastic energy between them. Based on the quantitative characterization of compatible martensite microstructure [23], the detected twin walls are mainly {110} type I/II for this alloy.

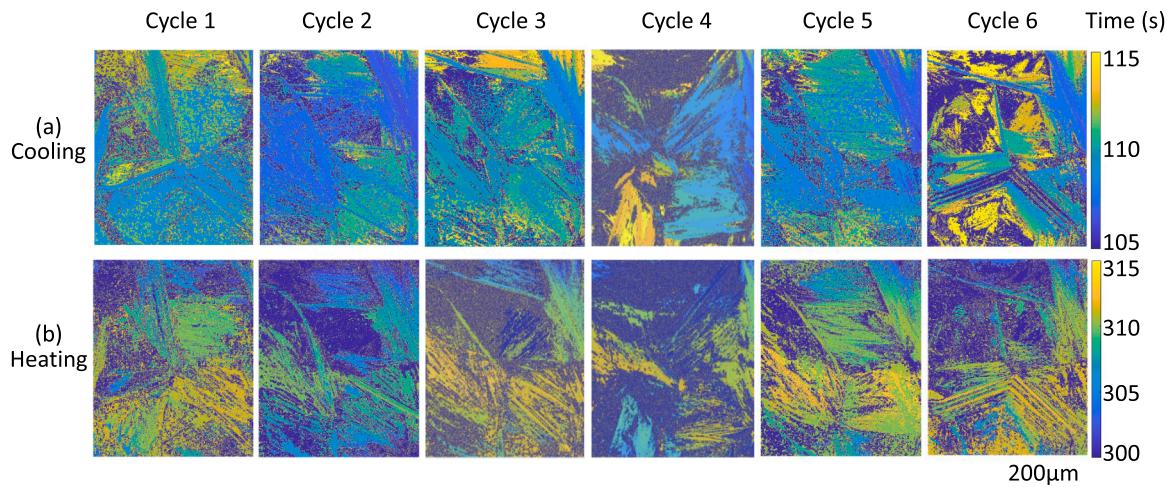Within a transformation temporal interval, we define the duration of phase transformation as

Fig. 3. Temporal evolution of martensite twinning structures within 15 seconds time intervals for all six thermal cycles during (a) cooling and (b) heating processes.
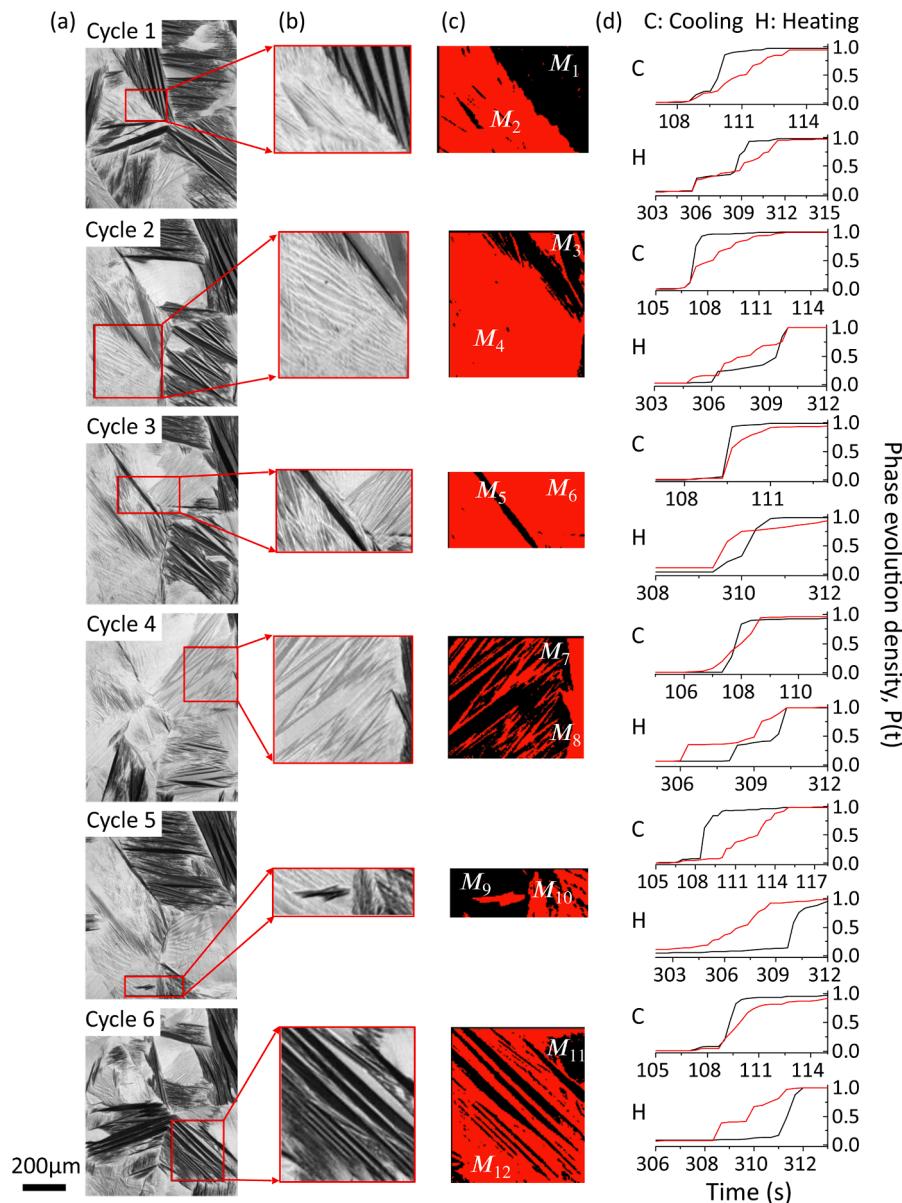
Fig. 4. (a) The fully developed martensite microstructure of $Au_{31}Cu_{24}Zn_{45}$ corresponding to (b) the selected sub-regions comprised of different types of twins. (c) Segmented coarse and fine morphology domains, where the black domain corresponds to the coarse microstructure, and red domain corresponds to the fine microstructure. (d) Phase evolution density $P_i(t)$ for each of the selected morphological domains during both heating/cooling processes.

$$\nu = \frac{t_{0.9} - t_{0.1}}{P(t_{0.9}) - P(t_{0.1})}, \tag{7}$$

where $t_{0.1}$ and $t_{0.9}$ are the times corresponding to 10% and 90% of new phase formed in the selected morphological domain. Within each of the morphological domains, we define the fineness as

$$w = \frac{|p|}{\ell}, \tag{8}$$

where $|p| = 1.25\mu m$ denotes the pixel size of the image, and ℓ in unit of μm is the mean twin spacing measured from the images in Fig. 4 (b). According to (8), the fineness w is a dimensionless parameter. Fig. 5 shows that the fineness and the time to form/vanish a twinning structure are linear, which can be fitted by

$$\nu = aw + b \tag{9}$$

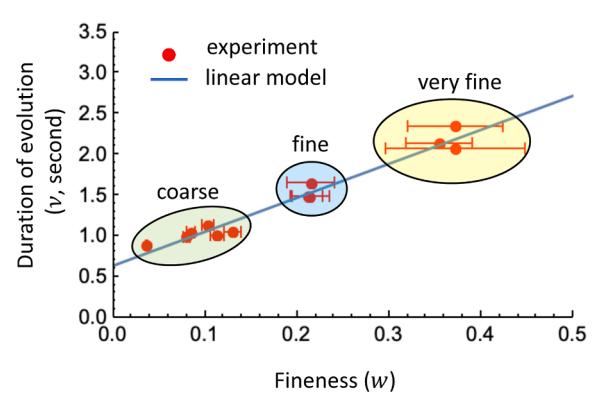with the fitting parameters $a = 4.713s$ and $b = 0.636s$. The mean

Fig. 5. The relationship between the fineness of microstructure and corresponding evolution duration. The error bars represent uncertainties of the measurement for the mean twin spacing.

5

squares error of the linear model in (9) is 0.00985. The uncertainties are primarily attributed to the fineness measurements of the martensitic twins within the selected morphological domains, especially for the very fine twins. The error bars in Fig. 5 present the length variation with regard to the mean twin spacing in each of the selected morphological domains. According to our morphological segmentation, we observe that three clusters agree well with the linear model given by (9), marked as coarse, fine and very fine in Fig. 5. For the very fine twins, the variation of twin widths is large compared to the coarse twins. Although very fine martensite twins exhibit relatively large deviation from the linear model, the overall trend of the model is clear: As the fineness $w \to 0$, $\nu \to b$ with a constant slope of a. The linear model predicts the formation time of zero-fineness martensite (*i.e.* twinless single variant) as the extrapolation to ν-axis in Fig. 5. In this material, the formation time of a single variant is estimated as 0.636 seconds. The linear term aw suggests the time cost for the twin laminates formation. Since the finite twin wall connects a pair of martensite variants through a rank-one relation, there is no elastic energy within the twin wall. We conjecture that the linear coefficient a is related to the characteristic time for the formation of twin laminates to overcome the interfacial energies. The transformation time of coarse microstructures is the half of the very fine microstructures. Since there exist many low-energetic compatible austenite/martensite interfaces for an alloy satisfying the cofactor conditions, we find that the martensite tends to form coarse twins to reduce the interfacial energy between martensitic variants, and the evolution time of twins scales linearly as their fineness. Although different types of twins are observed in consecutive thermal cycles, the microstructure evolution still follows this scaling law.

In summary, we introduced an in situ thermal-microstructural characterization method to study a phase transforming alloy $Au_{31}Cu_{24}Zn_{45}$ that satisfies the cofactor conditions. Utilizing the differential interference contrast microscope to a differential scanning calorimetry instrument, we are able to characterize the thermal properties and the formation of microstructure of the transforming alloy simultaneously. We verified that the transformation events indexed by the DInM image are well synchronized with the thermal events at phase transformation during both heating/cooling processes. We observed that the coarse microstructure forms more suddenly and more rapidly than the fine microstructure. Although the morphology and the fineness of martensite twins seem to form randomly from cycle to cycle, we showed that the twin evolution should linearly scale as its twin spacing, and we determine the characteristic time for the transformation.

Declaration of Competing Interest

The authors declare that they have no known competing financial interests or personal relationships that could have appeared to influence the work reported in this paper.

Acknowledgments

Supplementary material

Supplementary material associated with this article can be found, in the online version, at doi:10.1016/j.scriptamat.2022.114831.

References

[1] X. Chen, V. Srivastava, V. Dabade, R.D. James, Journal of the Mechanics and Physics of Solids 61 (2013) 2566–2587.
[2] Y. Song, X. Chen, V. Dabade, T.W. Shield, R.D. James, Nature 502 (2013) 85.
[3] X. Ni, J.R. Greer, K. Bhattacharya, R.D. James, X. Chen, Nano letters 16 (2016) 7621–7625.
[4] J. Jetter, H. Gu, H. Zhang, M. Wuttig, X. Chen, J.R. Greer, R.D. James, E. Quandt, Physical Review Materials 3 (2019) 093603.
[5] A. Evirgen, I. Karaman, R. Santamarta, J. Pons, C. Hayrettin, R. Noebe, Acta Materialia 121 (2016) 374–383.
[6] E.L. Pang, C.A. McCandler, C.A. Schuh, Acta Materialia 177 (2019) 230–239.
[7] Y. Liang, S. Lee, H. Yu, H. Zhang, Y. Liang, P.Y. Zavalij, X. Chen, R.D. James, L. A. Bendersky, A.V. Davydov, X. Zhang, I. Takeuchi, Nature communications 11 (2020) 1–8.
[8] C. Chluba, W. Ge, R.L. de Miranda, J. Strobel, L. Kienle, E. Quandt, M. Wuttig, Science 348 (2015) 1004–1007.
[9] H. Gu, L. Bumke, C. Chluba, E. Quandt, R.D. James, Materials Today 21 (2018) 265–277.
[10] M.S. Wechsler, D.S. Lieberman, T.A. Read, Trans. AIME (1953) 1504.
[11] J.S. Bowles, J.K. Mackenzie, Acta Metall. 2 (1954) 129–137.
[12] J.S. Bowles, J.K. Mackenzie, Acta Metall. 2 (1954) 138–147, https://doi.org/10.1016/0001-6160(54)90103-0.
[13] D.S. Lieberman, T.A. Read, M.S. Wechsler, J. Appl. Phys. 28 (1957) 532.
[14] J.S. Bowles, C.M. Wayman, Metall. Trans. 3 (1972) 1113.
[15] K.M. Knowles, D.A. Smith, Acta Metall. 29 (1980) 101.
[16] K.M. Knowles, D.A. Smith, Acta Metall. 29 (1981) 1445.
[17] R. Delville, S. Kasinathan, Z. Zhang, J.V. Humbeeck, R.D. James, D. Schryvers, Philos. Mag. 90 (2010) 177–195.
[18] Y. Wang, A.G. Khachaturyan, Acta Mater. 45 (1997) 759.
[19] V.I. Levitas, D.-W. Lee, D.L. Preston, Int. J. Plast. 26 (2010) 395–422.
[20] R.V. Kohn, S. Müller, Philos. Mag. A 66 (1992) 697–715.
[21] R.V. Kohn, S. Müller, Commun. Pure Appl. Math. 47 (1994) 405–435.
[22] X. Chen, N. Tamura, A. MacDowell, R.D. James, Applied Physics Letters 108 (2016) 211902.
[23] M. Chapman, M. De Graef, R.D. James, X. Chen, Philosophical Transactions of the Royal Society A 379 (2021) 20200112.
[24] R. Niemann, J. Kopeček, O. Heczko, J. Romberg, L. Schultz, S. Fähler, E. Vives, L. Mañosa, A. Planes, Physical Review B 89 (2014) 214118.
[25] E. Faran, D. Shilo, Shape Memory and Superelasticity 1 (2015) 180–190.
[26] Z. Zeng, C. Zhang, S. Du, X. Chen, Journal of the Mechanics and Physics of Solids 124 (2019) 102–114.
[27] Z. Zeng, H.-C. Chiu, L. Zhao, T. Zhao, C. Zhang, M. Karami, H. Yu, S. Du, X. Chen, Journal of the Mechanics and Physics of Solids 145 (2020) 104162.
[28] B. Pan, H. Xie, Z. Wang, Applied optics 49 (2010) 5501–5509.
[29] J. Cui, Y.S. Chu, O.O. Famodu, Y. Furuya, J. Hattrick-Simpers, R.D. James, A. Ludwig, S. Thienhaus, M. Wuttig, Z. Zhang, I. Takeuchi, Nat. Mater. 5 (2006) 286–290.
[30] Z. Zhang, R.D. James, S. Müller, Acta Mater. 57 (2009) 4332–4352.